Caving 2026 – A van As, D Cumming-Potvin & J Wesseloo (eds)

doi:10.36487/ACG_repo/2645_63

Estimating a block cave yield zone shape using comprehensive microseismic data

Denver Julian Birch [a,*], Stephen Guy Meyer [b], Gouri Sanekr Pararath [c], Jack Pilkington [c], Cristian Orrego [c], Arvic Osorio [c], Hassan Haayat [c]

[a] *Institute of Mine Seismology, Australia*

[b] *Institute of Mine Seismology, Canada*

[c] *Newmont Corporation, Australia*

Abstract

Estimating the shape of a developing cave remains an integral part of block cave mining. A growing cave perturbs the in situ stress field and induces seismic events, which in turn carry with them valuable information that can be used to formulate a more complete geomechanical model of the mine. Constraining the evolution of the yield zone has implications for forecasting the seismic hazard and improving the ability of numerical models to predict instabilities.

The utility of microseismic data is limited by sensor array characteristics and overall quality of data processing. As a result, case studies often present interpretations based on a subset of available methods, from basic locations of event hypocentres to more advanced tomographic imaging using body wave travel times.

This paper presents a unified, balanced framework using multiple sources of information derived from microseismic data to provide a comprehensive estimate of the yield zone around an Australian block cave mine with high-quality seismic data. The result is compared to other measurements such as cave tracking beacons and open holes.

Keywords: *microseismic, cave tracking, yield zone, seismic moment tensors, travel-time tomography*

1 Introduction

Microseismic monitoring remains a popular and efficient method for tracking cave progression due to the relatively low installation and operational costs, greater versatility and well-established technologies. Additional benefits of a microseismic monitoring system include monitoring of seismically active geological structures that may generate large seismic events (Orrego et al. 2024), monitoring seismicity associated with highly stressed pillars and abutments (Malovichko et al. 2018), or quantifying the demand on ground support (Malovichko 2023). However, mines that use microseismic data typically limit the analysis to estimates of event hypocentres and source parameters (radiated seismic energy, apparent stress, etc.). There have been many advances in how seismic data is routinely processed to provide information about the rock mass failure process (Malovichko 2022). Numerous routines that were previously considered advanced in microseismic monitoring are successfully automated today. As a result, effective seismic analysis with a well-designed and functioning sensor array produces multiple sources of readily available data to better interpret the rock mass condition with respect to the various stages of caving (Bayar et al. 2024). In addition to a general underutilisation of available data, there are currently no industry guidelines specifying how data from different monitoring methods should be applied to delineate the various zones associated with caving (Kamp et al. 2024).

[*] Corresponding author. Email address: denver.birch@imsi.org

The appropriate use of seismic data and need for an industry standard were identified by the Cave Mining 2040 (CM2040) Consortium, led by Mining3 and the University of Queensland. One of the projects sponsored under the CM2040 Horizon 1 phase dealt specifically with developing a tool that uses various forms of data in a repeatable manner, removing user bias where possible (Meyer 2023). The methods and data presented in this paper are built around the CM2040 tool.

Cadia East mine has a history of demonstrating effective practices for cave tracking using microseismic monitoring (Lynch et al. 2018). This work presents another example of that, involving the Cadia East PC2-3 extension (Orrego et al. 2020) to demonstrate how the CM2040 cave tracking framework is applied. A previously unused data source is introduced to extend the CM2040 framework, and a new mesh fitting routine is proposed. The resulting yielded zone boundary is finally compared with measurements from Geo4Sight tilt markers and open hole observations.

2 Data sources from routine seismic monitoring

The ability to effectively track spatial and temporal changes in the condition of the rock mass related to block cave mining relies fundamentally on the quality of processed seismic data. Geophones need to be correctly installed, adequately spaced and distributed above the cave back, such that the number of source-receiver pairs with line-of-sight is maximised. A sufficiently high system sensitivity is required and should be evenly distributed throughout the target volume. This greatly improves the accuracy in best estimates of the event hypocentres, source parameters and moment tensor solutions.

Such a system operates at Cadia Valley Operations at the Cadia East PC2-3 block cave extension where a competent rock mass and high seismic system sensitivity (magnitude of completeness: $M_W \leq -1.0$) produces thousands of events per month, approximately 40% of which have reliable moment tensor solutions. As a result, a variety of input data for cave tracking can be extracted from the dataset. A sample dataset consisting of 17,077 events (6,634 moment tensor solutions) recorded over a 3-month period is shown in Figures 1a–f in plan and section views. The concentration of data throughout the volume of interest can be described as highly variable. This is not unusual, as the recorded seismic response, while largely dependent on characteristics of the seismic system, also depends on the rock mass condition and redistribution of stress above the cave back as caving progresses.

Sources of input data (seismic parameters) that can be used to constrain the shape of a yield zone in block caving operations are well documented in various case studies (Glazer et al. 2005; Hudyma et al. 2008; Abolfazlzadeh & Hudyma 2016; Kamp et. al. 2024). These most often include event hypocentres, source parameters and tomographic imaging using measured body wave travel times (Mercier et al. 2015; Kamp et al. 2022; Hidayat et al. 2024). Less frequently used data sources include principal strain axes from moment tensor solutions (Lynch et al. 2018), tomographic imaging based on seismic attenuation, ambient noise or an active source (Meyer 2023), shear-wave splitting (Wuestefeld et al. 2011) and, as presented in this paper, back-projected P-wave polarisation vectors.

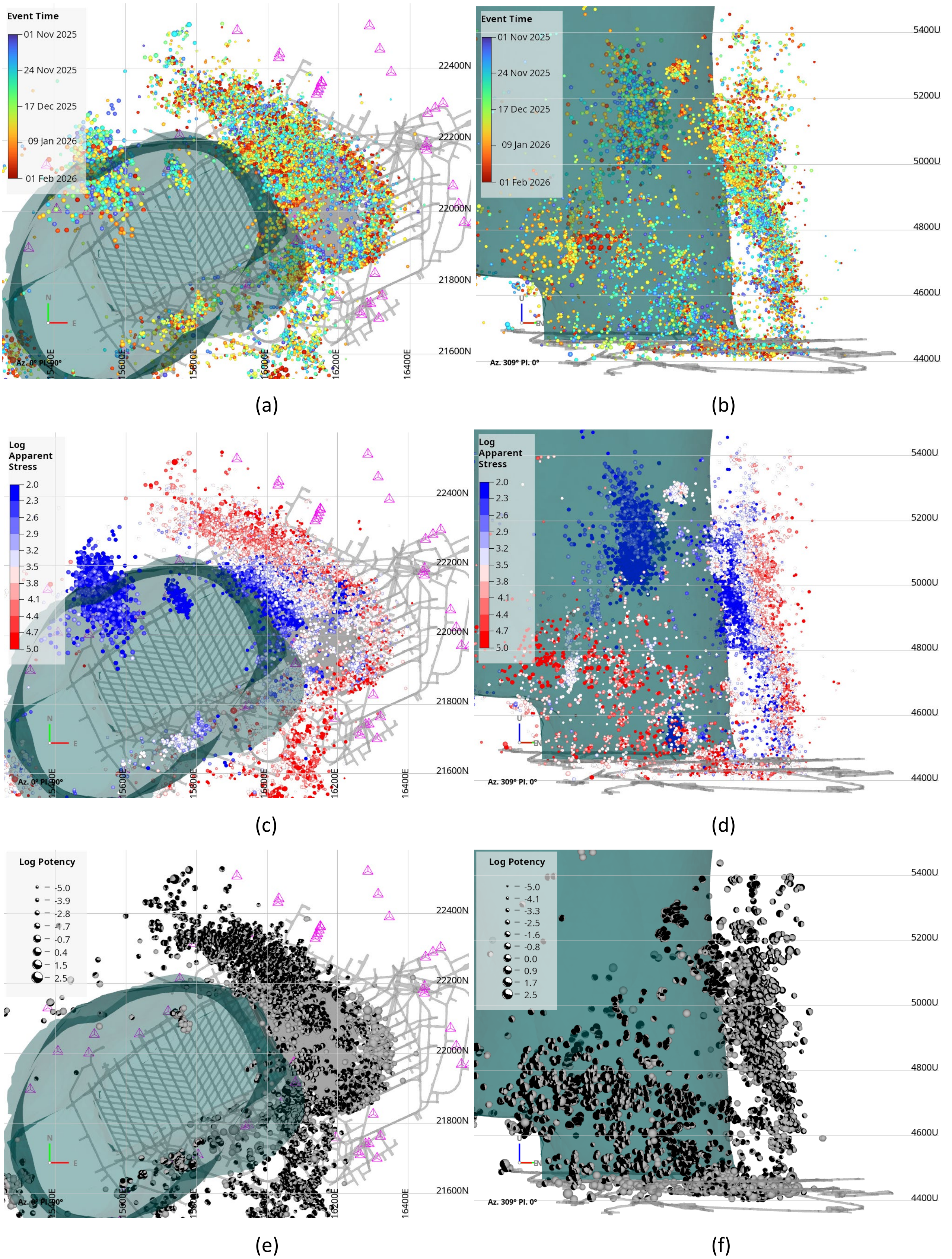

Figure 1 Sample dataset depicting results of routine seismic monitoring at Cadia East Mine, PC2-3 extension over 3 months. Spheres are coloured according to time (a–b), $\log$(Apparent Stress) (c–d) and displayed as beachballs (e–f)

The input data for cave tracking can be divided into two classes. The first provides point-source information at the estimated hypocentre of the seismic event and the second provides information about the medium between source and receiver. While these classes traditionally form the basis of independent analysis, a more complete 3D estimate of the yield zone can be obtained by combining this information.

Potential sources of data for cave tracking and the corresponding geomechanical relationships with the process of caving are summarised as follows:

- Seismic event locations (hypocentre estimates): the expectation is that as the cave propagates, so does the cloud of seismic event hypocentres ahead of the yield zone. Thus, the closest event to the centre of the cave is likely to be adjacent to the yield zone boundary where maximal damage is expected.
- Source parameters: as damage in the rock mass (fracture density) increases and confinement decreases, seismic events radiate less energy. Therefore, mapping spatial variations in derived source parameters such as Energy Index or Apparent Stress (which reflect radiated energy per unit potency) serves as a reliable indicator of proximity to the yield zone.
- Seismic moment tensors: it has become standard practice at most well-instrumented mines with competent, highly stressed rock masses to automatically evaluate seismic moment tensors (Malovichko 2022). Each moment tensor contains information about the shape, size and orientation of failure at the hypocentre. The expected stress field perturbations from a block cave, which drives brittle failure adjacent to the yielded zone, are typically well understood. For a seismic event near the yielded zone, the direction of σ_1 and therefore the expected direction of maximum compressional strain (represented by the P-axis) is expected to be parallel to the boundary. At the same time, the direction of dilation (T-axis) is expected to be approximately perpendicular (Lynch et al. 2018; Birch & Meyer 2019; Birch et al. 2022).
- Tomographic imaging and associated gradient: body wave travel times, ambient noise or calculated seismic attenuation (Q) are all related to differences in rock mass quality and stress. The nature of these relationships does not need to be exactly quantified to be useful. As fracture density increases and stress decreases (a yielded zone develops), seismic scattering attenuation increases and seismic velocities decrease. The spatial variation of these parameters is therefore useful to track yield zone growth over time. Travel-time tomography using the simultaneous iterative reconstruction technique (SIRT) (Jaimes et al. 2025) is executed automatically every month at Cadia East. Meyer (2023) notes the utility in mapping, not only absolute values, but also the associated gradients to illuminate sharp transitions in rock mass condition.
- Shear-wave splitting: shear-wave splitting is a geophysical phenomenon where an incoming, linearly polarised S-wave separates into fast and slow waves due to anisotropy in the rock mass. Caving in hard rock mines induces fractures parallel to the shape of the yield zone (Cumming-Potvin et al. 2018), accentuating shear-wave splitting. The technique was successfully applied in an Australian mine during block caving operations (Wuestefeld et al. 2011) but has not been widely adopted. This is likely due to the trade-off between the time required to implement the method and how much can be gained from it. Success relies heavily on data quality, availability of triaxial geophones and sensor geometry. As the yield zone develops, the availability of useful source-receiver pairs may diminish.
- P-wave polarisation: first-arriving P-waves typically deviate around yielded material. Therefore, plotting back-projected straight-rays based on the measured P-wave polarisation (incidence angle) is a simple means to illuminate possibly undisturbed material. Conversely, the volume enclosed by the straight-rays (i.e. an 'inner' volume) represents possibly yielded material.

2.1 Generalisation of input data

Combining complementary input data produces a more complete picture of the cave geometry, as mentioned in Section 2. To establish a statistically rigorous framework, all inputs must first be converted into some generalised parameter. Meyer (2023) proposes a simple grid-based approach that assumes some generic parameter, α_{ij}, for input type, i, at grid point, j, where a value of 1 represents completely yielded material and 0 represents completely intact. A confidence level, β_{ij}, is introduced to accommodate uncertainties related to the individual inputs. A final grid is constructed from a weighted combined criterion, where:

$$\alpha_j = \sum \omega_i \alpha_{ij} \text{ for points that satisfy } \beta_{ij} > C \quad (1)$$

The conversion from a raw input type to a generalised parameter follows some simple logic based on the expected geomechanical relationship between the measured input and state of the rock mass near the cave. Interpreting spatial data (e.g. event locations, moment tensors, ray paths) requires that a reference location be defined somewhere near the middle of the cave, $\bar{P}$, and radius of influence, r, for assigning seismic events to grid points.

The procedure to generalise hypocentre estimates is depicted in Figures 2a and 2b. If we consider all events within some distance, r, from a grid point, we can assign a rating based on how many are closer to $\bar{P}$ than to the grid point itself. If all events are further from $\bar{P}$, the associated grid point has a high score and vice versa. For source parameters, a grid point is simply assigned a rating based on an average relative energy measure (Energy Index or Apparent Stress, depending on user preference) from the events within r.

The use of moment tensor data, depicted in Figure 2c, relies on the directions of dilation (T axes). These are converted to cave-side pointing unit vectors defined using $\bar{P}$ and compared with the direction to an associated grid point. Taking the dot product yields values of −1 to 1 for each moment tensor within r. Summing these and normalising between 0 and 1 provides a corresponding rating. In all three examples, a confidence level can depend on the number of observations or parameter uncertainty estimates.

Figure 2d depicts the logic behind the use of tomography data. The same would apply to other grid-based data where a selected range of values map linearly onto a range of α values.

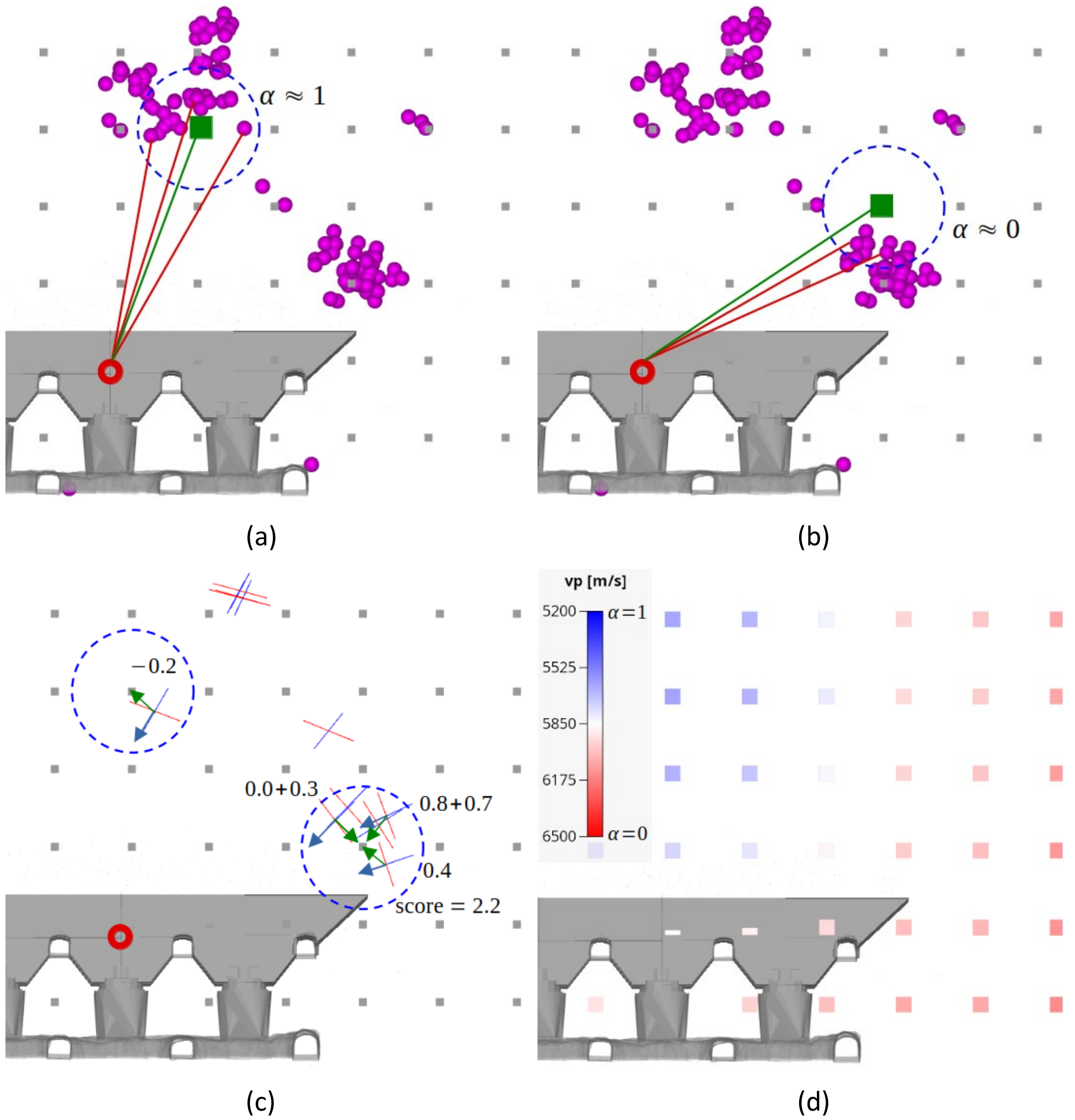

Figure 2 Demonstrative examples showing how inputs are generalised onto a regular grid. (a, b) Event hypocentre estimates; (c) Principal strain axes from moment tensor solutions; (d) P-wave velocity model from travel-time tomography

2.2 P-wave polarisation for yield zone tracking

As described in Section 2, back-projected straight-rays based on the measured P-wave polarisation can illuminate the perturbed rock mass associated with caving. This concept is illustrated in Figure 3a. There is a clear dependence on the positioning of source-receiver pairs similar to what applies to measurements of shear-wave splitting and tomographic imaging techniques. Figure 3b shows the concept applied to real data at Cadia East. The visible polarisation vectors (straight-ray paths) have lengths equal to half the source-receiver distances and correspond to first arrivals with signal-to-noise ratios greater than 10 and angular deviations, as defined in Figure 1a, greater than 20°.

A new method to estimate a generalised parameter for inclusion in the CM2040 framework was required. The approach is similar to converting moment tensor data, described in Section 2.1. Polarisation vectors intersecting a radius, r, from each grid point are classified as either in front or behind using the dot product of two unit vectors originating at the grid point: one directed along the shortest path to the intersecting vector, and the other pointing towards the cave reference point, $\bar{P}$. Figure 3c shows an example of the results when the method is applied to real data.

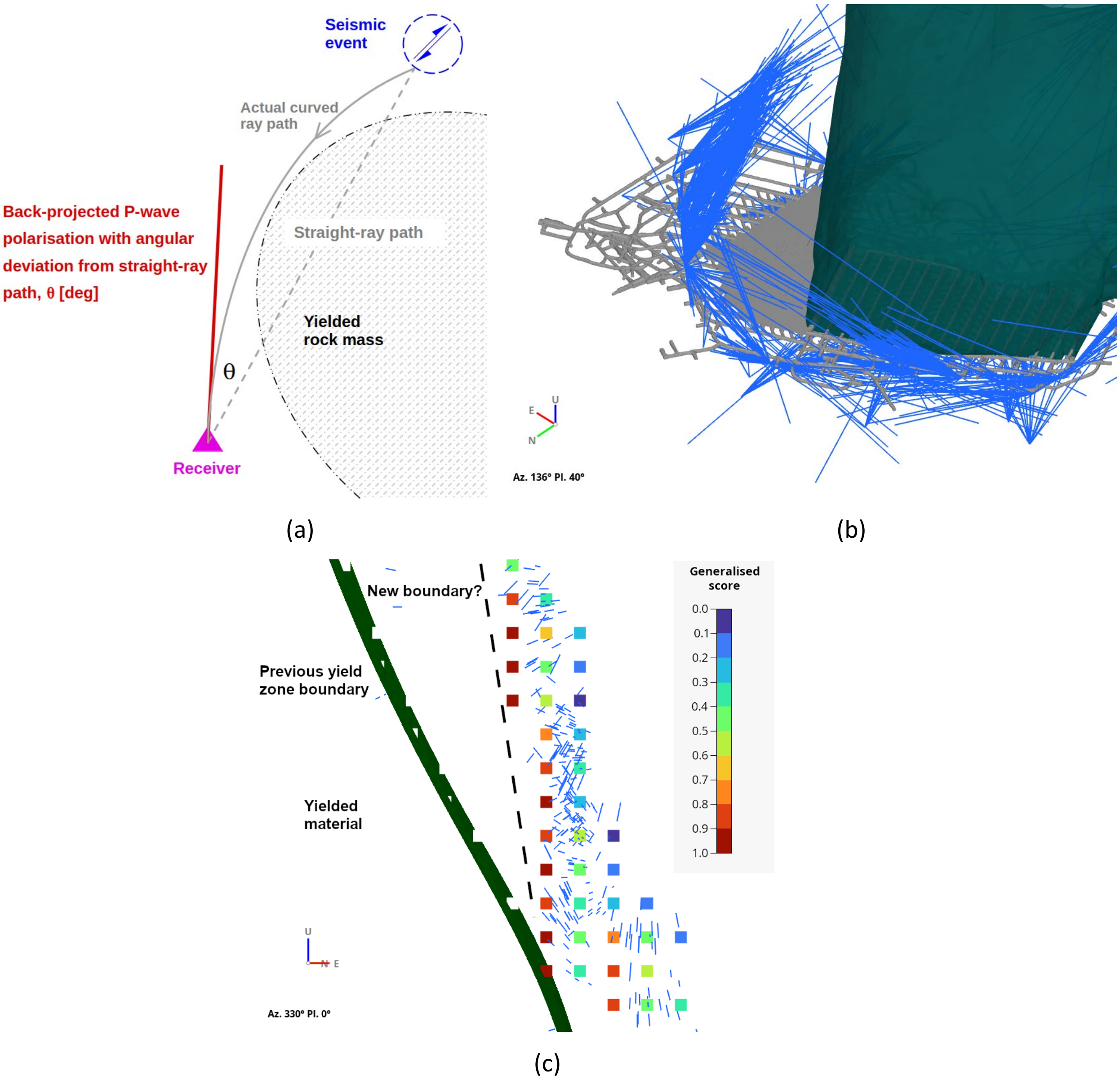

Figure 3 Conceptual sketch depicting the relationship between (a) a back-projected straight-ray path, measured from P-wave polarisation, and yielded rock mass, (b) visualisation using real data from Cadia East, PC2-3 extension, and (c) associated scoring in section view showing a potential update to the yield zone shape based on polarisation data alone

3 Practical application

This section demonstrates how a variety of inputs are combined to map cave progression at the Cadia East PC2-3 extension. This is typically conducted on a quarterly basis. The grid geometry and cave reference point needed for generalisation are depicted in Figure 4. Note that we are attempting to fit a northeasterly extension of an existing shape. The reference point was therefore positioned slightly southwest of the abutment. Available input types are listed in Table 1. If a particular grid point has missing data with respect to one type of input, for example, no source mechanisms nearby, the contribution to the combined value is 0 and the maximum possible value the point can obtain is less than 1. Results from the generalisation procedures for each of the six inputs are plotted in section view in Figures 5a–f, with a combined result presented in Figure 6.

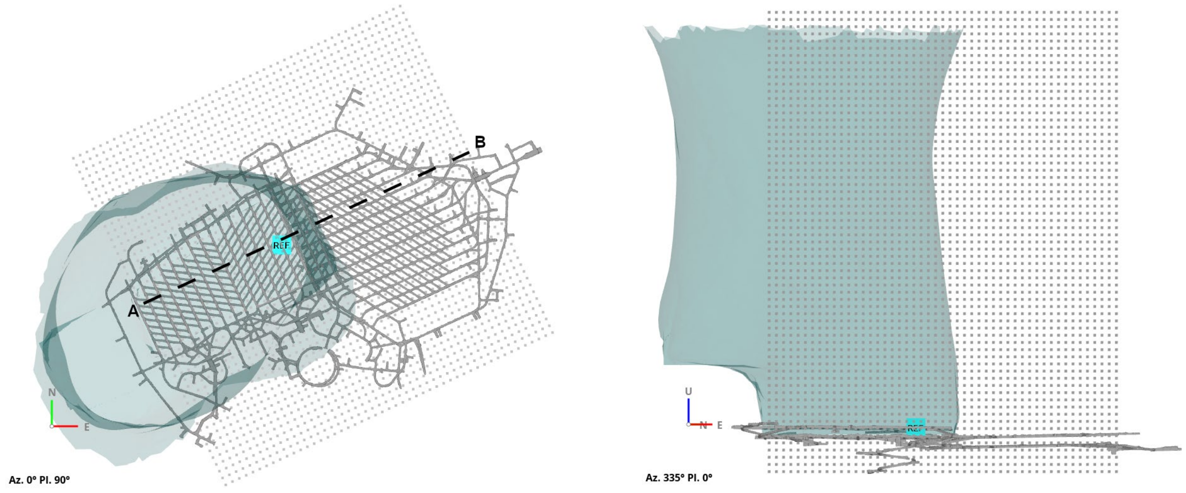

(a) (b)

Figure 4 Target volume with regular grid (20 × 20 × 20 m) and a reference point for generalising the cave tracking inputs in (a) plan and (b) section view. The results in Figure 5 were plotted in the A-B plane

Table 1 Cave-tracking inputs and their associated impact in terms of the number of contributing grid points and custom-assigned weighting

Input type	Number of contributing grid points	Weighting
Event hypocentre estimates	7,688	0.2
Source parameters	11,304	0.2
Moment tensor solutions	5,636	0.2
P-wave polarisation vectors	2,485	0.2
P-wave velocities from body wave travel-time tomography using SIRT (Jaimes et al. 2025)	155,668	0.1
Gradient of P-wave velocities	96,358	0.1

The complementary nature of the input types becomes apparent on inspection of Figure 5. For example, a gap left by moment tensor data in Figure 5c is covered by the polarisation vector results in Figure 5d. This makes the approach more robust than relying on the strengths and weaknesses of one source of information like travel-time tomography, for example.

The results in Figures 5a and 5b relating to event hypocentres and source parameters have a relatively large spread in the upper sections, which negatively impacts the search for a discrete boundary in the final combined score (Figure 6). While it is tempting to dismiss this as an artefact of hypocentre estimation uncertainty, basic inspection of the processing results and the fact that it is confined to the upper parts where cave growth is actively occurring suggest the spread is genuine.

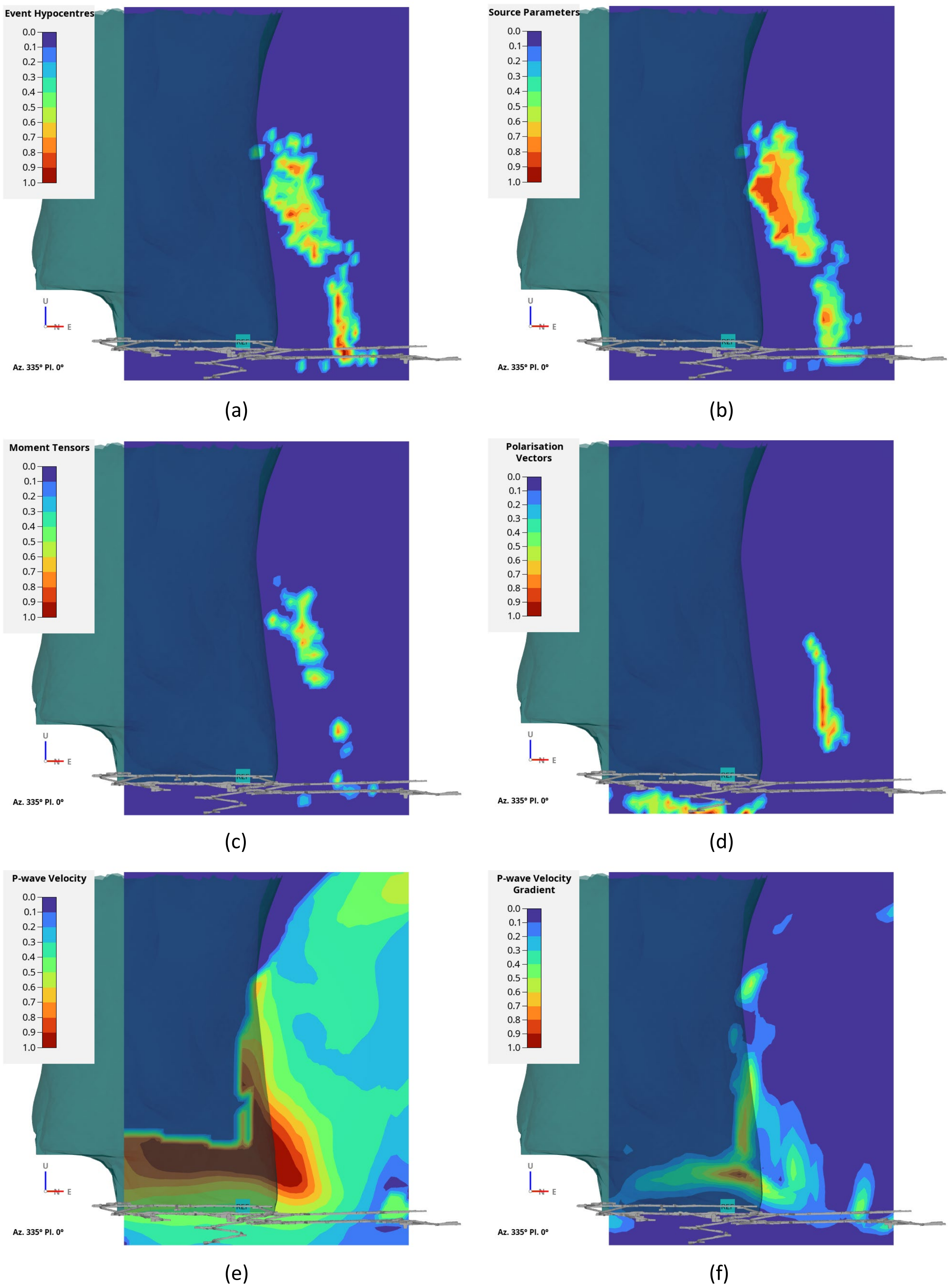

Figure 5 Results following generalisation of cave-tracking inputs listed in Table 1 plotted in the A-B plane depicted in Figure 4a

The results in Figure 5b reflect lower energy events nearest the cave interior progressing to higher energies at the outer boundary, reminiscent of the conceptual model for caving proposed by Duplancic & Brady (1999). This does not discount the fracture banding mechanism for cave growth described by Cumming-Potvin et al. (2018). In fact, both mechanisms are supported by the data. Figure 7a shows how the timing and spatial distribution of events resembles the observations from Cumming-Potvin et al. (2018), while the source parameters in Figure 7b support the notion of a continuous rock mass damage profile.

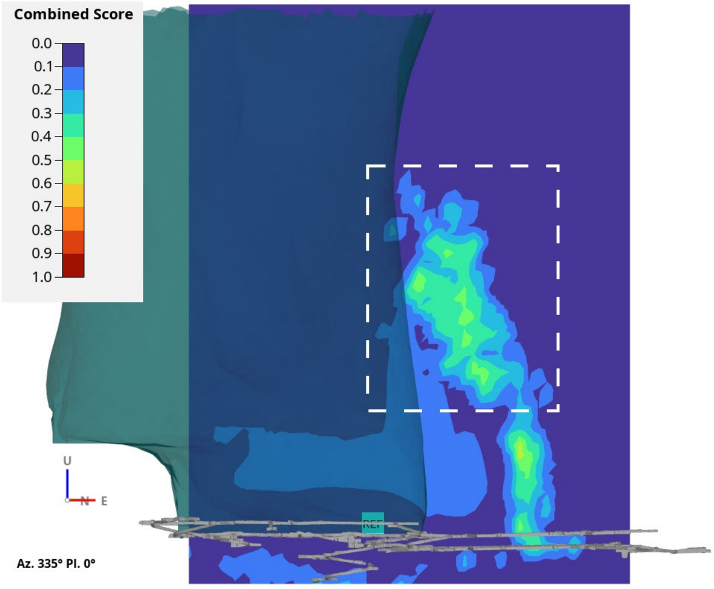

Figure 6 Combined score plotted in the A-B plane based on weighting listed in Table 1. The rectangle outlines the area depicted in Figure 7

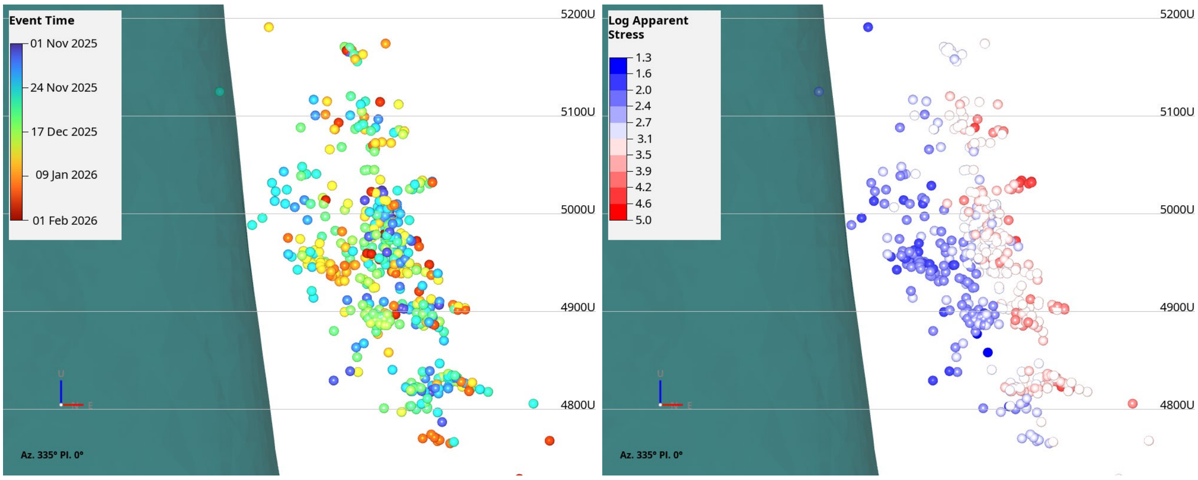

(a) (b)

Figure 7 Seismic events related to cave growth within 10 m either side of the A-B plane. Spheres are coloured according to time (a) and the logarithm of Apparent Stress (b)

4 Towards standardised shape-fitting

Interpreting available data for the purpose of tracking cave growth without a standardised approach is highly subjective. The procedure described in Section 2 and demonstrated in Section 3 is a significant step forward; however, the final hurdle of fitting a shape remains elusive. Shapes are usually manually extrapolated. Practitioners may produce drastically different shapes for consecutive periods, rely on limited data, mimic the results of numerical stress models or simply throw out observations that do not fit expectations.

Measuring cave progression accurately is essential to managing various risks that can be catastrophic, e.g. managing the air blast hazard or estimating the influence of the yield zone on stress redistribution in the abutment using numerical modelling. To assist with this, we developed a novel routine prototype with an interactive graphical user interface to systematically generate shapes based on the combined output from Section 3 (Figure 6), thereby reducing subjectivity and allowing for repeatability with a limited number of traceable user inputs.

The following steps are involved in the fitting procedure:

1. Smoothing: We employed a spatial moving-average technique, recalculating each data point based on the mean value of its local neighbours within a defined radius (Figure 8).
2. Filtering: A threshold is applied to the smoothed grid of combined scores.
3. Removing outliers: Density-based clustering is applied to identify and remove disconnected clusters using a maximum distance threshold.
4. Curve fitting and mesh generation: Refer to Figures 9a–c. A weighted mean radial distance is calculated to generate 2D horizontal boundary curves at discrete Z-intervals. The individual curves are then lofted together to generate a continuous 3D mesh surface. The algorithm strictly constrains the boundary geometry to circular or ellipsoidal profiles to mitigate instability caused by sparse or clustered data. The final mesh surface is constrained by three primary inputs:
   a. Fixed centre axis that dictates the absolute centre of rotation for all curves.
   b. Elevation smoothing window to blend data between elevations.
   c. Dynamic angular coverage (wrap) percentage that enables scaling between a circular or ellipsoidal arc. For example, if coverage is less than this value, the algorithm will attempt to fit a circular arc to the data.

Figures 9a–c present the elements described in point 4 above. The use of circular and elliptical 2D boundary curves was selected over more complex routines, such as b-spline interpolation, to better constrain the behaviour in areas with few data. Another major advantage to the approach is the means to track which settings were used in the process, as depicted in Figure 9c. However, there are improvements outstanding, such as the integration of non-seismic data and implementing a stable method to fit the top part of the yield zone for caves that have not yet broken through.

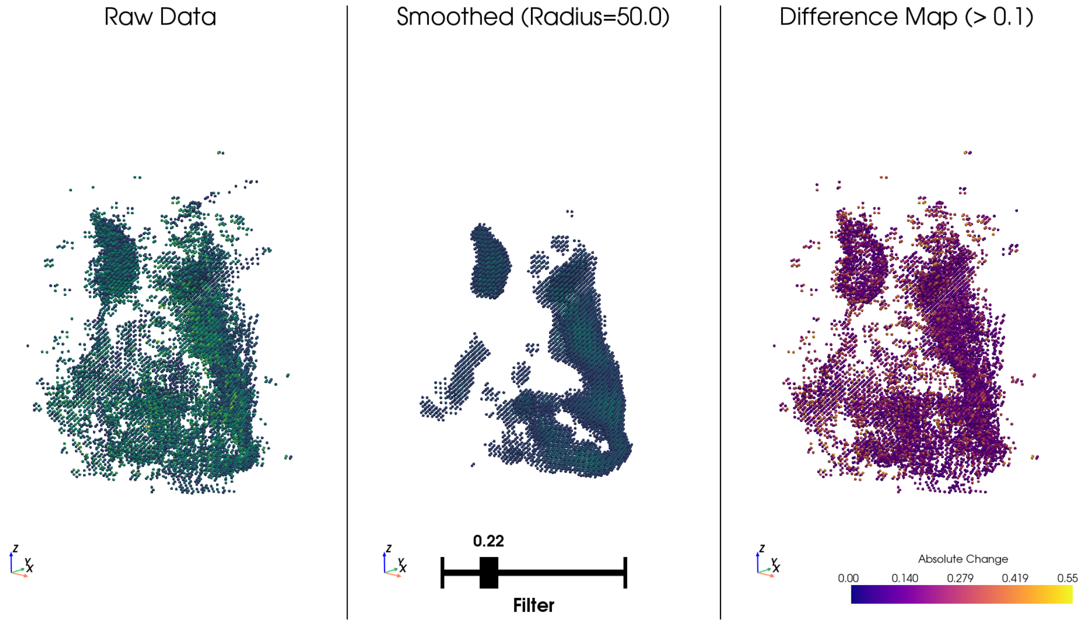

Figure 8 Results of smoothing using a 50 m spatial moving average applied to gridded data from the combined output in Section 3 (Figure 6). Results are depicted in 3D for scores higher than 0.22

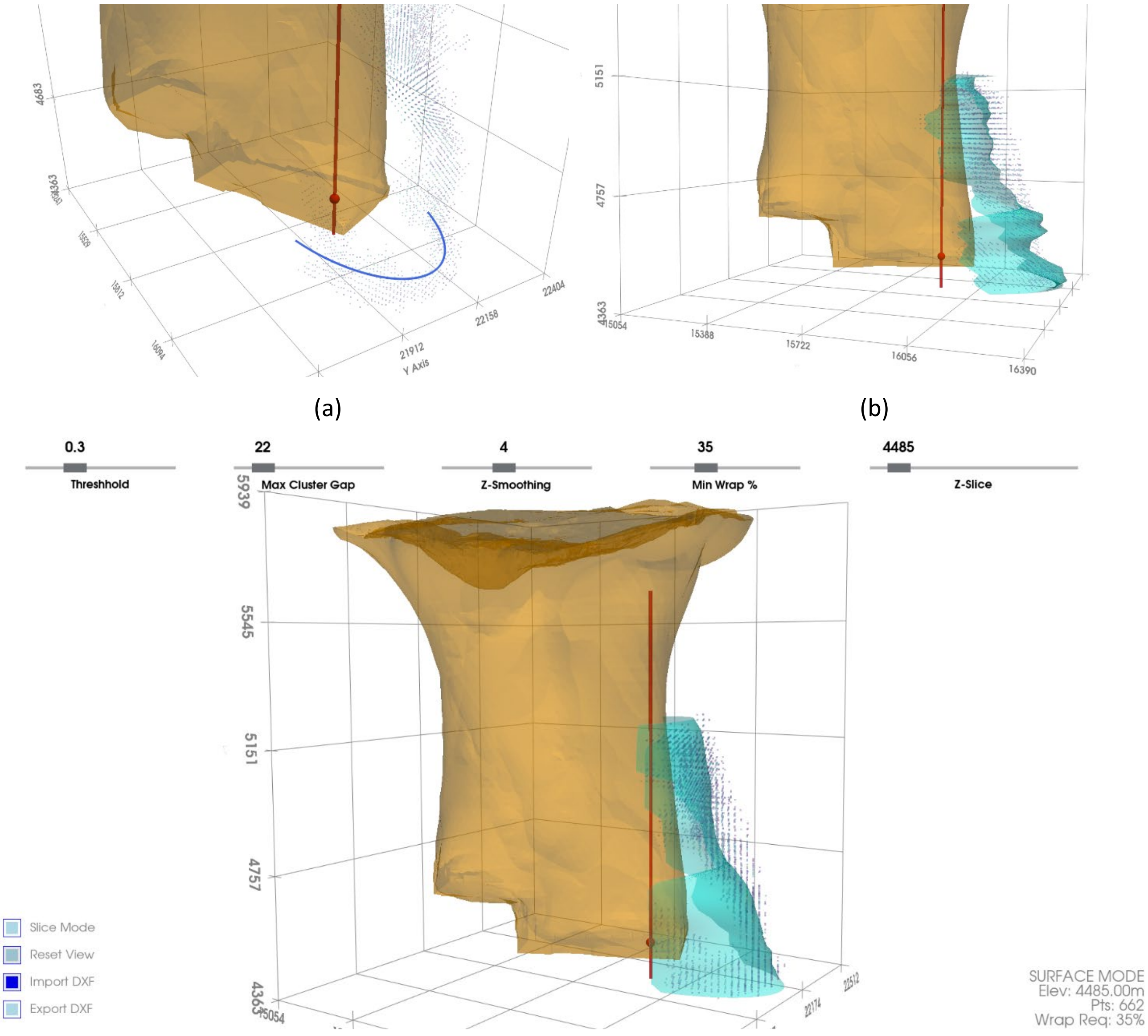

Figure 9 Snapshots illustrating the surface-fitting procedure. The orange surface is a pre-existing yield zone boundary, and the blue represents the PC2-3 extension. (a) Each Z-interval is fitted by an elliptical or circular arc (yellow line) relative to the reference axis; (b) Result without elevation smoothing, and (c) Final shape with interactive sliders displaying the chosen settings

5 Comparison with non-seismic data sources

It is possible to integrate non-seismic data for the purpose of estimating a yield zone boundary shape but since the objective of this paper is to rely on the results of microseismic monitoring, non-seismic data sources serve as a comparison to the interpolated shape of the yield zone boundary in Figure 9c.

5.1 Open holes and tilt measurements

Open holes are boreholes which are surveyed using a downhole borehole camera to assess the condition and continuity of the rock mass. Open holes drilled into the cave column continue to serve as an important source of qualitative geotechnical information for assessing cave behaviour, fracture zone development and the evolving rock mass response. While open hole data cannot independently define cave geometry, the data provide direct observational evidence that is valuable for verifying and comparing other inferred datasets used to characterise cave propagation.

Monitoring of open holes intersecting the yielded zone has revealed clear signs of structural degradation, including multiple dislocations, offsets and localised blowouts along the hole length. These features reflect progressive deformation of the surrounding rock mass as stresses redistribute and the cave-related fracture zone develops. Several open holes monitoring the PC2-3 extension demonstrate intermittent 'breathing' or air-suction behaviour. This behaviour indicates that permeable pathways exist between the hole and the cave, providing indirect evidence of active fracturing within the rock mass.

The Geo4Sight tilt markers are deployed in underground boreholes at a fixed 2 m spacing and fully grouted to measure subsurface deformation using triaxial tilt sensors and positional changes based on Received Signal Strength Indicator (RSSI). The tilt measurements at the PC2-3 extension generally show a similar pattern of a gradual increase, followed by a period of relative quiescence, then rapid acceleration and finally loss of communication (i.e. consumption). This behaviour is interpreted as follows:

- The gradual increase in tilt indicates a transition from intact to yielding conditions.
- Relative quiescence reflects a period during which deformation is uniformly distributed in the volume.
- Acceleration in tilt thereafter reflects intensified dilation and low confinement ultimately ending in detachment.

Figure 10 shows the results of open hole and tilt measurements for the corresponding yield zone shape interpolation. The largest recorded tilt measurements for each marker and the deepest positions of open hole dips are shown. There is good agreement with four of the open hole dip positions (green spheres) situated within 50 m from the external yield zone boundary. The large gap between Geo4Sight markers in one of the holes was attributed to a loss of battery power. There is some correlation with tilt although the values reflect highly localised rock mass damage intensities, making it difficult to establish a defined boundary.

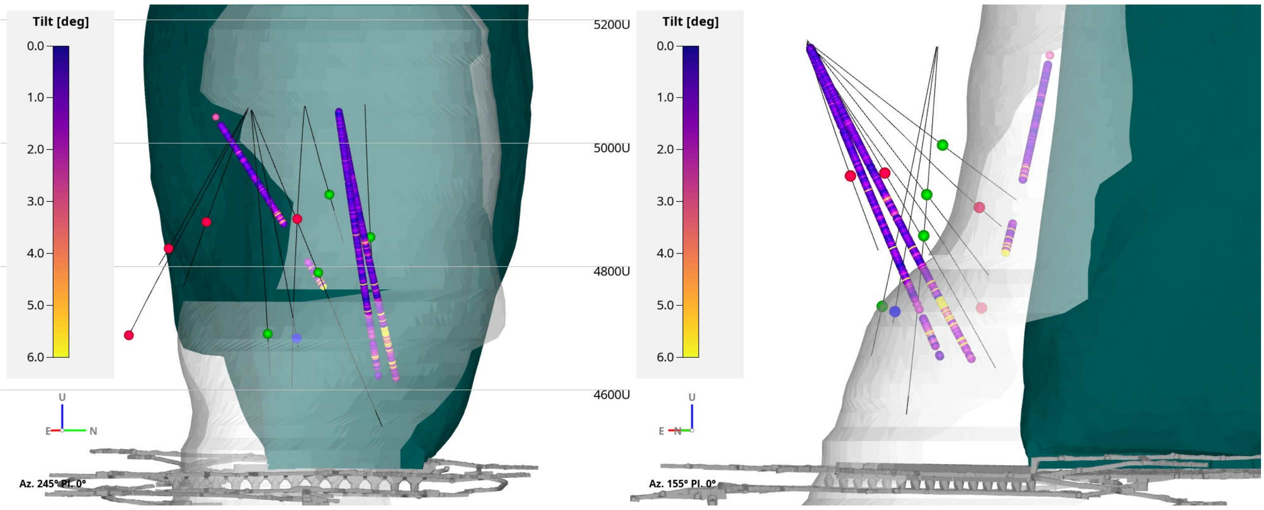

(a) (b)

Figure 10 Tilt and open hole measurements plotted against the interpolated shape of the yield zone boundary. Open holes are marked as black lines with coloured dip positions. Green points are less than 50 m from the fitted mesh shape, red are more than 50 m, and blue indicates inside

6 Conclusion

Accurate tracking of cave propagation is critical in block cave mining for managing geotechnical risks, forecasting seismic hazards and validating numerical models. Historically, estimating the 3D volume of yielding related to block cave mining has relied heavily on manual extrapolation, which can lead to subjective and inconsistent geomechanical assessments.

This paper presents a comprehensive, multi-parameter framework developed under the CM2040 initiative to delineate the external yield zone boundary with improved reliability. Demonstrated using high-quality microseismic data from the Cadia East PC2-3 extension, the methodology successfully integrates six complementary inputs: event hypocentres, source parameters, moment tensors, P-wave polarisation vectors, P-wave velocities from travel-time tomography, and velocity gradients. By converting these inputs into a generalised, grid-based scoring system combined with confidence weightings, the framework effectively mitigates the inherent blind spots and uncertainties associated with relying on any single data source. For instance, spatial gaps left by moment tensor data can be covered by polarisation vector results, yielding a far more robust 3D representation of the rock mass condition.

To overcome the subjectivity of manual boundary interpretation, a novel, interactive shape-fitting routine was introduced. The algorithm involves a combination of spatial smoothing, filtering, density-based clustering, and rigorous geometric constraints (using circular or elliptical arcs) to generate a continuous, repeatable 3D surface mesh of the yield zone boundary.

The derived boundary was compared to open hole and tilt measurement data. The interpolated yield zone shape shows reasonably good agreement with open hole camera penetration depths, matching within 50 m of the external boundary in parts. Tilt measurements show a general trend of increasing intensity with depth but remain a difficult measure point for cave tracking due to discontinuous temporal and spatial progression, likely reflecting the true nature of cave propagation. The absence of an available ground-truth shape precluded a quantitative comparison. Furthermore, such a comparison remains inherently challenging without a universally adopted, measurement-based definition of the yield zone boundary – highlighting a critical area for future research.

Ultimately, the unified framework represents a significant step in cave tracking by standardising data interpretation, reducing user bias and leveraging a larger range of routinely available microseismic data. Future development will focus on directly integrating non-seismic instrumentation into the shape-fitting process and improving boundary resolution for the upper limits of caves prior to surface breakthrough.

Acknowledgement

The authors gratefully acknowledge Newmont for supporting this work and granting permission to publish these results. We also extend our thanks to the Cave Mining 2040 Consortium, led by Mining3 and the University of Queensland, for driving research into new technologies for cave mining.

Disclaimer

This paper is for informational and academic discussion purposes only and is strictly site-specific to Newmont’s Cadia East operations. The multi-parameter frameworks, 3D mesh shape-fitting routines, and microseismic generalisation methods (including CM2040 tool applications) involve inherent geomechanical uncertainties and are based on localised operational variables. Newmont Corporation makes no warranties, express or implied, regarding the accuracy of these spatial interpolations or their applicability to other mining environments. Any reliance on or replication of these methodologies by third parties is done entirely at their own risk, and Newmont expressly disclaims all liability for resulting operational outcomes, property damage or injury. Nothing herein constitutes investment advice or a solicitation regarding Newmont securities.

References

Abolfazlzadeh, Y & Hudyma, M 2016, 'Identifying and describing a seismogenic zone in a sublevel caving mine', *Rock Mechanics and Rock Engineering*, vol. 49, no. 9, pp. 3735–3751.

Bayar, E, Simanjuntak, K, Birch, D, Mardiansyah, F & Purwanto, H 2024, 'Seismological data and analysis for the early stages of block caving', in D Johansson & H Schunnesson (eds), *MassMin 2024: Proceedings of the International Conference & Exhibition on Mass Mining*, Luleå University of Technology, Luleå, pp. 893–908, https://doi.org/10.36487/ACG_repo/2435_G-02

Birch, DJ & Meyer, SG 2019, 'Seismic response to hydraulic fracturing in caving mines', in W. Joughin (ed.), *Deep Mining 2019: Proceedings of the Ninth International Conference on Deep and High Stress Mining*, The Southern African Institute of Mining and Metallurgy, Johannesburg, pp. 445-460, https://doi.org/10.36487/ACG_rep/1952_33_Birch

Birch, D, Basson, G & Rigby, A 2022, *Yield Zone Tracking (Year 3)*, internal report, Institute of Mine Seismology Research Programme, Project A-YZT.

Cumming-Potvin, D, Wesseloo, J, Jacobsz, SW & Kearsley, E 2018, 'A re-evaluation of the conceptual model of caving mechanics', in Y Potvin & J Jakubec (eds), *Caving 2018: Proceedings of the Fourth International Symposium on Block and Sublevel Caving*, Australian Centre for Geomechanics, Perth, pp. 179–190.

Duplancic, P & Brady, B 1999, 'Characterisation of caving mechanisms by analysis of seismicity and rock stress', in G Vouille & P Berest (eds), *International Congress on Rock Mechanics Proceedings*, vol. 2, CRC Press, Boca Raton, pp. 1049–1053.

Glazer, SN & Hepworth, N 2005, 'Seismicity induced by cave mining, Palabora experience', in Y Potvin & M Hudyma (eds), *RaSiM6: Proceedings of the Sixth International Symposium on Rockburst and Seismicity in Mines Proceedings*, Australian Centre for Geomechanics, Perth, pp. 281–289, https://doi.org/10.36487/ACG_repo/574_26

Hidayat, W, Sahara, DP, Widiyantoro, S, Suharsono, S, Riyanto, E, Nukman, M, … Putra, IPRA 2024, '4D time lapse tomography for monitoring cave propagation and stress distribution in Deep Mill Level Zone (DMLZ) PT Freeport Indonesia', *Geomechanics and Geophysics for Geo-Energy and Geo-Resources*, vol. 10, article no. 39, https://doi.org/10.1007/s40948-023-00718-w

Hudyma, M, Potvin, Y & Allisons, D 2008, 'Seismic monitoring of the Northparkes lift 2 block cave-part I undercutting', *Journal of The South African Institute of Mining and Metallurgy*, vol. 108, no. 7, pp. 405–419.

Jaimes, A, Rigby, A, Birch, DJ & Lotter, EC 2025, 'Noninvasive imaging of the underground via travel-time tomography: overview and recent developments', *11th International Symposium on Rockbursts and Seismicity in Mines*, pp. 337–355.

Kamp, C, Conley, A, Collins, DS, Preiksaitis, M, Butler, T & Shumila, V 2022, 'Use of seismic tomography to aid rock mechanics interpretation at New Afton B3 block cave mine', in Y Potvin (ed.), *Caving 2022: Proceedings of the Fifth International Conference on Block and Sublevel Caving*, Australian Centre for Geomechanics, Perth, pp. 461–472, https://doi.org/10.36487/ACG_repo/2205_31

Kamp, C, Cumming-Potvin, D, Lett, J, Poulter, M, Shea, N, Jalink, B & Vanegas-Palacio, C 2024, 'Cave profile interpretation using instrumentation and the cave conceptual model', in D Johansson & H Schunnesson (eds), *MassMin 2024: Proceedings of the International Conference & Exhibition on Mass Mining*, Luleå University of Technology, Luleå, pp. 318–349, https://doi.org/10.36487/ACG_repo/2435_C-02

Lynch, R, Meyer, S, Lotter, E & Lett, J 2018, 'Tracking cave shape development with microseismic data', in Y Potvin & J Jakubec (eds), *Caving 2018: Proceedings of the Fourth International Symposium on Block and Sublevel Caving*, Australian Centre for Geomechanics, Perth, pp. 555–564, https://doi.org/10.36487/ACG_rep/1815_43_Lynch

Malovichko, D, Cuello, D & Rojas, E 2018, 'Analysis of damaging seismic event on 24 December 2011 in the Pilar Norte sector of El Teniente mine', in Y Potvin & J Jakubec (eds), *Caving 2018: Proceedings of the Fourth International Symposium on Block and Sublevel Caving*, Australian Centre for Geomechanics, Perth, pp. 637–650, https://doi.org/10.36487/ACG_rep/1815_49_Malovichko

Malovichko, DA 2022, 'Utility of seismic source mechanisms in mining', *10th International Symposium on Rockbursts and Seismicity in Mines*, pp. 1–27.

Malovichko, D 2023, 'Utilisation of seismic data in the assessment of displacement and energy demand imposed on ground support by strainbursts', in J Wesseloo (ed.), *Ground Support 2023: Proceedings of the 10th International Conference on Ground Support in Mining*, Australian Centre for Geomechanics, Perth, pp. 181–196, https://doi.org/10.36487/ACG_repo/2325_12

Mercier, J-P, de Beer, W, Mercier, J-P & Morris, S 2015, 'Evolution of a block cave from time-lapse passive source body-wave traveltime tomography', *Geophysics*, vol. 80, no. 2, pp. WA85–WA97.

Meyer, S 2023, 'Cave front tracking using active and passive microseismic data', *Cave Mining 2040 Consortium for Global Cave Mining Research: Horizon 1 Outcomes*.

Orrego, C, Lowther, R & Newcombe, G 2020, 'Undercutting method selection at Cadia East PC2-3 extension', in R Castro, F Báez & K Suzuki (eds), *MassMin 2020: Proceedings of the Eighth International Conference & Exhibition on Mass Mining*, University of Chile, Santiago, pp. 370–384, https://doi.org/10.36487/ACG_repo/2063_23

Orrego, C, Viegas, G, Tennant, D & Stonestreet, P 2024, 'Geological and historically based numerical assessment of seismic hazard in an evolving block cave mine', in P Andrieux & D Cumming-Potvin (eds), *Deep Mining 2024: Proceedings of the 10th International Conference on Deep and High Stress Mining*, Australian Centre for Geomechanics, Perth, pp. 1179-1192, https://doi.org/10.36487/ACG_repo/2465_77

Wuestefeld, A, Kendall, JM, Verdon, JP & van As, A 2011, 'In situ monitoring of rock fracturing using shear wave splitting analysis: an example from a mining setting', *Geophysical Journal International*, vol. 187, no. 2, pp. 848–860, https://doi.org/10.1111/j.1365-246X.2011.05171.x